HHS Public Access

Author manuscript

J Immunol. Author manuscript; available in PMC 2022 July 22.

Published in final edited form as:

J Immunol. 2021 March 15; 206(6): 1228–1239. doi:10.4049/jimmunol.2000967.

FATC domain deletion compromises ATM protein stability, lymphocyte development, and promotes lymphomagenesis

Maja Milanovic[1], **Zhengping Shao**[1], **Verna M. Estes**[1], **Xiaobin S. Wang**[1,2], **Demis Menolfi**[1], **Xiaohui Lin**[1], **Brian J. Lee**[1], **Jun Xu**[5], **Olivia M. Cupo**[1], **Dong Wang**[5], **Shan Zha**[1,2,3,4]

[1]Institute for Cancer Genetics, Vagelos College of Physicians and Surgeons, Columbia University, New York City, NY 10032

[2]Department of Pathology and Cell Biology, Vagelos College of Physicians and Surgeons, Columbia University, New York City, NY 10032

[3]Division of Pediatric Oncology, Hematology and Stem Cell Transplantation, Department of Pediatrics, Vagelos College of Physicians & Surgeons, Columbia University, New York City, NY 10032

[4]Department of Immunology and Microbiology, Vagelos College of Physicians & Surgeons, Columbia University, New York City, NY 10032

[5]Skaggs School of Pharmacy & Pharmaceutical Sciences, University of California San Diego, La Jolla, CA 92093

Abstract

ATM kinase is a master regulator of the DNA damage response and loss of ATM leads to primary immunodeficiency and greatly increased risk for lymphoid malignancies. The FATC domain is conserved in Phosphatidylinositol-3-kinase-related protein kinases (PIKKs). Truncation mutation in the FATC domain (R3047X) selectively compromised reactive oxygen species-induced ATM activation in cell-free assays. Here we show that in mouse models, knock-in ATM-R3057X (Atm^{RX}, corresponding to R3047X in human ATM) mutation severely compromises ATM protein stability, and causes T cell development and B cell immunoglobulin class switch recombination defects and infertility resembling ATM-null. The residual ATM-R3057X protein retains minimal, yet functional measurable, DNA damage-induced checkpoint activation and significantly delays lymphomagenesis in $Atm^{RX/RX}$ mice compared to $Atm^{-/-}$. Together, these results support a physiological role of the FATC domain in ATM protein stability and show that the presence of minimal residual ATM-R3057X protein can prevent growth retardation and delay tumorigenesis without restoring lymphocyte development and fertility.

Address Correspondence to Shan Zha at sz2296@cumc.columbia.edu.

Author contributions

ZS, VME, and SZ generated the ATM-R3057X mouse models. VME performed the initial analyses of the first few RX mice. MM completed the analyses of lymphocyte development, lymphomagenesis, DNA damage responses. DM performed additional DNA damage response measurements during revision. BJL and CO helped chimer generation, germline transmission, and colony management. BJL carefully proofread the manuscript. XW and DM constructed the HTGT-seq library. XW performed the initial mapping, filtration, and bioinformatic analyses of the HTGT-seq. MM further analyzed and visualized the HTGTS data using the visual basic tool developed by ZS. XL performed the Southern blotting for the hybrid and coding joint formations. JX and DW provided the in-silica model of the ATM kinase domain. MM and SZ wrote the manuscript.

The authors declare no conflict of interest.

Keywords

ATM; R3047X; FATC domain; CSR; and lymphomagenesis

Introduction

Ataxia-Telangiectasia (A-T) Mutated (ATM) is a protein serine/threonine kinase and a master regulator of the DNA damage response (DDR) (1). Germline inactivation of ATM causes A-T syndrome, characterized by extreme sensitivity to ionizing radiation, cerebellar degeneration, and loss of fertility (2). Nearly 70% of A-T patients show immunodeficiency (3, 4). ATM null mice do not develop spontaneous ataxia but recapitulate the immunodeficiency of A-T patients (5–10).

At the cellular level, ATM kinase is recruited to and activated by the MRE11-RAD50-NBS1 (MRN) complex at the site of DNA damage (11). Activated ATM promotes efficient and accurate DNA double-strand break (DSB) repair. In developing lymphocytes, loss of ATM compromises physiological DNA DSBs repair during V(D)J recombination (12, 13), underlying the T cell development block in A-T patients and ATM-deficient mice (8). Loss of ATM abolished the residual V(D)J recombination in cells lacking XLF, a non-essential non-homologous end-joining (NHEJ) factor (13–16). ATM also plays an important role in DSB repair during immunoglobulin class switch recombination (CSR) (17–19), during which naïve B cells express antibodies with effector function thus different isotypes (*e.g.*, IgG1 or IgE, instead of the initially expressed IgM) (20). Loss of ATM reduces CSR efficiency by ~50% (17, 18, 21) and leads to the accumulation of DSBs at IgH locus in ~30% of activating B cells (22), underlying the humoral/antibody defects in A-T patients (3, 4). High-throughput sequencing of CSR junctions recovered from ATM-deficient B cells reveals a significant more and longer microhomology at the junctions (19), suggesting a role of ATM in NHEJ-mediated repair of CSR breaks. In addition to lymphocyte development, ATM is also required for meiotic recombination in germ cells (23–25). A-T patients and ATM-deficient mice are sterile (26). Activated ATM phosphorylates p53, Chk2, and others to activate DNA damage-induced cell cycle checkpoints (27). The checkpoint function of ATM is critical for its tumor suppressor role (1). About 25% of A-T patients develop lethal lymphoid malignancies (28). Almost all ATM null mice (5–10) succumb to lethal thymic lymphomas with recurrent t(12:14) translocations involving the TCRα/σ locus (10, 29, 30). In addition to DNA damage, purified ATM can also be activated by reactive oxygen species (ROS) in an MRN-independent process that requires the formation of disulfide bond between the C2991 residues of two ATM monomers (31). While brain tissues from A-T patients show signs of protein and lipid oxidation (32–36), the physiological role of ROS-induced ATM activation remains elusive, in part due to the lack of mouse models that can distinguish ROS vs. DNA damage-induced ATM activation (31, 37).

ATM belongs to the phosphatidylinositol 3-kinase-related kinase (PIKK) family that also includes ATR, DNA-PK, and mTOR kinases (38). They all contain a conserved kinase domain followed by a PIKK regulatory domain (PRD) and a ~33 amino acids FATC domain (39). Structure studies suggest an allosteric activation model, in which the conserved

Kα9 and Kα10 helices in the PRD physically block the substrate and ATP from entering the catalytic center (40–42). Indeed, PRD contains several residues implicated in ATM activation, including the C2991 (31) involved in disulfide-bond mediated ATM activation by ROS, K3016 (43) implicated in DNA damage-induced acetylation of ATM, and S2996 (44) an autophosphorylation site [Fig. 1A and 1B]. The FATC domain (ATM amino acid 3023–3056) includes a conserved α-helix and a flexible tail. The FATC domain of DNA-PK and mTOR are essential for their respective kinase activity (45, 46). Truncating mutation with the ATM FATC domain (R3047X) selectively ablates ROS-induced, but not MRN and DNA-induced activation of purified ATM protein (31). To understand the physiological role of the FATC domain, we generated a mouse model carrying the knock-in R3057X (corresponding to R3047 in human ATM, Atm^{RX}) mutation. Our analyses reveal a critical role of the FATC tail in ATM protein stability and indicate that growth retardation and lymphomagenesis are more sensitive to residual ATM kinase activity, while lymphocyte development, CSR, and germ cell development requires substantial ATM kinase activity.

Materials and Methods

Mouse models and generation of the $Atm^{Rx/Rx}$ mouse model

The $Atm-/-$ mouse model was described previously (47). To generate the $Atm^{RX/RX}$ mouse carrying the R3057X truncating mutation (NP_031525.3, corresponding to R3047X of human ATM) [Fig. 1A and 1B], the 3.5 kb 5’ arm and the 3.9 kb 3’ arm were amplified from genomic DNA extracted from CSL5 embryonic stem cells (129/sv background). The mutation was introduced in the 3’ arm and cloned into the pEMC targeting vector carrying a neomycin-resistant (NeoR) cassette flanked by FRT sites, each containing XbaI sites for identification [Fig. S1A]. The correct targeting clones have the NeoR upstream of the R3057X mutation site (CGA (Arg)-> TGA (stop)) in exon 62 [Fig. S1A and S1C] and were identified by Southern Blotting upon XbaI digestion using a 3’ probe generated by PCR (primers, 5’-TCT CCT GGC TAC ATG CTA-3’ and 5’-AAC ACT CAG CCG TCG TC-3’) [Fig. S1B]. The expected germline (GL) band is ~7.7 kb and the correctly targeted band is ~4.3 kb (with the insertion of NeoR) [Fig. S1B]. The mutation was confirmed by Sanger sequencing [Fig. S1C]. Two clones were independently injected for germline transmission and yielded identical phenotypes. They were discussed together thereafter. The resulting chimeras were bred with *Rosa26aFLP/FLP* mice (the Jackson Laboratory; stock no. 003946) to remove the NeoR cassette. Tail DNA from $Atm^{RX/RX}$ mice were PCR amplified and sequenced to confirm the desired mutations. Genotyping was performed with primers (FWD 5’- CGC ACA GTG TCG TCT G-3’ and REV 5’- CGT GCC TTT TAA TTA TGT AG-3’) and the Atm^{RX} allele was identified by a 592 bp PCR product vs. a 474 bp product for the germline allele. The $Atm^{RX/RX}$ mice used in this study were all in a 129/Sv background. All animal work was conducted in a specific pathogen-free facility and all the procedures were approved by the Institutional Animal Care and Use Committee at Columbia University Medical Center.

Lymphocyte development and Class switch recombination

Lymphocyte development and CSR were performed as described before (48–50). Briefly, ~1×10^5 nucleated 0Tcells from lymphoid organs of 5–8-week-old mice were stained with

fluorescence-conjugated antibodies and analyzed on a FACS Calibur flow cytometer (BD Biosciences). The specific antibodies used were: PE-CD4 (clone GK1.5, BD Pharmingen, 553730), FITC-CD8α (clone 53–6.7, BioLegend, 100705), APC-TCRβ (clone H57–597, BD Pharmingen, 553174), PE/Cy7 TER-119 (BioLegend, 116222), FITC-CD43 (clone S7, BD Pharmingen, 553270), PE-Cy5-B220 (clone RA3–6B2, BD Pharmingen, 553091) and PE-IgM (Southern Biotech, 1020–09). For CSR, $CD43^{-}$ B cells were isolated from total splenocytes after depletion with anti-CD43 magnetic beads (MACS, Miltenyi, 130–049-801) and cultured at ~1×10^6 0Tcells ml^{-1} Pin RPMI (Gibco, 11875–093) supplemented with 15% fetal bovine serum (Hyclone, SH30071.03), 1x MEM non-essential amino acids (Gibco, 11140–050), 20 mM HEPES (Gibco, 15630080), 2 mM L-glutamine (Gibco, 25030–081), 1x penicillin/streptomycin (Gibco, 15140122), 120 μM 2-mercaptoethanol (Fisher, 034461–100), and IL-4 (20 ng/mL; R&D, 404-ML-050) and anti-CD40 (1 μg/mL; BD Bioscience, 553721). Cultured cells were maintained daily at ~1×10^6 0Tcells ml^{-1} and collected daily for flow cytometry analyses with FITC-conjugated IgG1 (clone A85–1, BD Pharmingen, 553443) and PECy5-conjugated B220 (clone RA3–6B2, BD Pharmingen, 553091). All flow cytometry data were analyzed using the FlowJo software package.

Generation of v-abl-transformed B cells, CTV analyses, and small chemicals

Murine Abelson virus-transformed B cells were generated by isolating total bone marrow from < 5 weeks old $Atm^{+/+}$ $Atm^{-/-}$ Pand $Atm^{RX/RX}$ mice and infecting them with a retrovirus encoding the v-abl kinase (12). Cells were cultured in DMEM (Gibco, 12430–054) supplemented with 15% fetal bovine serum (Hyclone, SH30071.03), 1x MEM non-essential amino acids (Gibco, 11140–050), 2 mM L-glutamine (Gibco, 25030–081), 1 mM sodium pyruvate (Gibco, 11360–070), 1x penicillin/streptomycin (Gibco, 15140122) and 120 μM 2-mercaptoethanol (Fisher, 034461–100) for the next 6–8 weeks to allow for the generation of the stable clones. For treatment with Tert-Butyl Hydroperoxide (TBH) solution, cells were incubated in media without 2-mercaptoethanol. The proliferation of primary B cells was analyzed using the Cell Trace Violet (CTV) kit (ThermoFisher Scientific, C34557) according to the manufacturer's protocol. Cells were analyzed by flow cytometry on an Attune NxT flow cytometer (ThermoFisher Scientific). The following small molecules were used at the concentrations indicated in the figure legends: TBH solution (Luperox TBH70X, Sigma, 458139), Colcemid (KryoMAX™ Colcemid™, Gibco, 15212–012), Neocarcinostatin (NCS) (Sigma, N9162).

PCR analysis of endogenous Hybrid joints

PCR analyses of hybrid joints were performed as previously described (12). PCR (50μl) was carried out with 75μm dNTPs and 15 pmol of each primer. Vκ6–23 HJs and CJs were amplified from the splenocyte DNA (0.5μg) using nested PCR The PCR condition for the first PCR was: 95°C 5 minutes, (94°C 30s- 64°C 30s- 72°C 30s) x17 with following primers –pκJa&pκ6a for HJ and pκJa and pκ6d for CJ. Secondary PCR was carried out under the same conditions (x25 cycles) with 1:4 serial dilutions of the first PCR products with primers – pκJa&pκ6b for HJ and pκJa and pκ6c for CJ (Supplementary Fig. 2G). Vβ14 HJs and CJs were amplified from thymocyte genomic DNA (0.5μg). For Vβ14 HJs, pβa&pβb was used for the 1st PCR, and pβc&pβd were used for the secondary PCR (same condition as above with annealing temperature at 55°C and extension time of the 60s). Vβ14 CJs and IL2 were

directly amplified from 4-fold serially diluted genomic DNA with the primers, pβe&pβf for Vβ14 CJs and IMR-042 and IMR-043 for IL2. The PCR condition was: 94°C 5 minutes, (94°C 30s, 60°C 30s, 72°C 30s) x30. PCR products were run on 1% TAE Gel followed by Southern blotting analysis with p^{32}-labeled oligonucleotide probes pβg for Vβ14 HJs and CJs, pκg1 for Vκ6–23 HJs and CJs, and IMR042–2 for IL2. Vk6–23 CJ band is 0.68 kb and Vk6–23 HJ band is 0.26 kb. Vβ14 CJ band is 0.3 kb and Vβ14 HJ bands are 0.9 kb. The primers used are listed in Supplementary Fig. 5.

Cell cycle analyses

For G2/M checkpoint analysis combining the anti-pH3 and BrdU staining [Fig. 6D-F], B cells undergoing CSR were collected at 2.5 days post-stimulation and left untreated or treated with NCS (100 ng/mL) for 1 hour. Cells were washed with PBS and then incubated in the presence of Colcemid (100 ng/ml final) for the next 3 hours. Half an hour before collection, cells were pulse-labeled with 10 μM of BrdU, then collected and fixed with 70% ethanol for 24 hours. The cells were permeabilized (0.3% Triton-X in PBS) and stained with an anti-phosphorylated Histone H3 (S10) (pH3) antibody (EDM Millipore, 06–570), followed by incubation with the secondary antibody Alexa594 (Invitrogen, A-11012). Cells were then neutralized (sodium phosphate citrate buffer, pH 7.4) before being stained with an anti-BrdU antibody (BD Pharmingen, 556028) according to the manufacturer's protocol. The stained cells were co-stained with propidium iodide (PI) (Sigma, P4170) for 30 minutes in the presence of Rnase A (Sigma, 10109169001). Cells were analyzed on an Attune NxT flow cytometer (Thermo Fisher Scientific) and the data were analyzed with Flowjo software package.

Western blotting and antibodies

For Western blotting, whole-cell extracts (WCEs) were prepared using modified RIPA buffer (150 mM sodium chloride, 10 mM Tris–hydrogen chloride pH 7.4, 0.1% sodium dodecyl sulfate, 0.1% Triton X-100, 1% sodium deoxycholate, 5 mM ethylenediaminetetraacetic acid) supplemented with 2 mM phenylmethylsulfonyl fluoride, 10 mM sodium fluoride, 10 mM β-glycerophosphate, and protease inhibitor cocktail (Roche, 11697498001). SDS-PAGE and immunoblots were performed following standard protocols. Primary antibodies used in the study are: anti-ATM (Sigma, A1106), anti-pKAP1 S824 (Abcam, ab70369), anti-KAP1 (Cell Signaling, 4124), anti-CHK2 (BD Biosciences, 611570), anti-pH2AX Ser139 (Cell Signaling, 9718S), anti-H2AX (Millipore, 07–627), anti-Vinculin (Millipore, 05–386), and anti-β-actin (Sigma, A1978). Image quantification was carried out using ImageJ. Briefly, pKAP1 and KAP1 bands were selected and measured for the area under the curve (arbitrary units). The data was presented as the ratio pKAP1/KAP1 (both area under the curve).

Metaphase spreads and telomere-FISH (T-FISH)

Metaphases were collected from activated B cells at 4.5 days after stimulation as previously described with 2 hours with Colcemid (100 ng/ml, KaryoMax™ Colcemid™ Solution, GIBCO) (51). Telomere FISH staining was performed as detailed before (51), counterstained with Vectashield +DAPI (Vector Laboratories, H-1200–10) and analyzed on a Carl Zeiss AxioImager Z2 microscope equipped with a CoolCube 1 camera and a

63×/1.30 oil objective lens, driven by Metafer4 and the ISIS fluorescence image software (MetaSystems).

HTGTS

HTGTS was carried out as previously described (19, 52–55). Briefly, DNA from activated B cells (4 days with IL4, anti-CD40) was sonicated to ~1000 bp (Diagenode Bioruptor), before amplified via an Sμ-specific biotinylated primer (5′/5BiosG/CAGACCTGGGAATGTATGGT3′). The biotinylated products were isolated with magnetic beads, ligated to an adaptor, and amplified with a nesting primer 5′CACACAAAGACTCTGGACCTC3′. Endonuclease AflII was used before the nesting PCR to remove the germline sequence. The libraries were sequenced on Illumina Miseq (150× 150 pair ended platform). Since all mice used here are of 129 background, we replaced the IgH switch region (from JH4 to the last Cα exon, chr12 114, 494, 415–114, 666, 816) of the C57/BL6-based mm9 with the corresponding region from 129sv (GenBank accession no. AJ851868.3) (1415966–1592715) to generate the mm9sr (switch region replacement) genome. The published HTGTS pipeline was used for mapping and filtration (19, 54). The best-path searching algorithm (related to YAHA; (56)) has been deployed to identify optimal sequence alignments from Bowtie2-reported top alignments (alignment score > 50). Mispriming events, germline (unmodified) sequence, sequential joints, and duplicated reads were removed. Duplication was defined by bait and prey alignment coordinates both within 2 nt of another read's bait and prey alignments. Reads unequivocally mapped to an individual S-region were recovered based on mappability filter (please see (54) for simulation and details on plotting). Microhomologies (MHs) are defined as sequences that can be assigned to both bait and prey. Insertions are regions that map to neither bait nor prey. The data were then plotted on excel using a visual basic tool (55, 57, 58). Sequence data have been deposited to GSE162568.

Results

Generation and characterization of the ATM R3057X mouse model

The R3057X (CGT-> CAT) mutation (corresponding to the R3047X at the FATC domain of human ATM [Fig. 1A and 1B]) was introduced into the endogenous *Atm* locus via homologous targeting [Fig. S1A]. The successfully targeted embryonic stem cell clones were identified by Southern blotting [Fig. S1B]. The mutation was confirmed by Sanger sequencing [Fig. S1C]. Two independently targeted embryonic stem cell clones were injected for germline transmission and analyzed together. $Atm^{+/RX}$ and $Atm^{RX/RX}$ mice were born at the expected Mendelian ratio [Fig. 1C]. In contrast to the smaller size of the $Atm^{-/-}$ mice, $Atm^{RX/RX}$ mice were of normal weight and had a similar rate of weight-gain as $Atm^{+/+}$ and $Atm^{+/RX}$ littermates [Fig. S1D and S1E]. Unexpectedly, Western blotting analyses of the splenic B cells from $Atm^{RX/RX}$ mice using a monoclonal antibody against amino acid 1967–1988 of human ATM (59), showed that ATM-RX protein level reduced ~ 10 fold from the ATM-WT control [Fig. 1D]. The severe reduction of the ATM-RX protein is mainly due to the loss of protein stability since the Atm-RX mRNA level is comparable to that of ATM-WT in $Atm^{+/RX}$ B cells [Fig. 1E]. R3057 is encoded in the last exon of the *Atm* gene [Fig. S1A], and R3057X should not be a candidate for non-sense mediated decay (60).

In agreement with the much-reduced ATM-RX protein level and the essential role of ATM in meiotic recombination (23–25), male $Atm^{RX/RX}$ mice have empty epididymis and lack mature spermatids in testes [Fig. 1F]. Taken together, these results suggest that the residual ATM-RX protein and activity can support normal weight, but not meiosis (26).

$Atm^{RX/RX}$ mice show defects in thymocyte development.

ATM kinase activity plays an important role in lymphocyte development (61). So next, we analyzed the lymphocyte development in young (5–7 weeks) $Atm^{RX/RX}$ mice. The total thymocyte count from the $Atm^{RX/RX}$ mice was not significantly lower than that of $Atm^{+/+}$ controls, while significantly reduced in $Atm^{-/-}$ mice [Fig. S2A]. Nevertheless, $Atm^{RX/RX}$ thymocytes showed a partial blockade at the CD4+CD8+ double-positive (DP) to CD4+ or CD8+ single-positive (SP) T cell transition [Fig. 2A, 2B, S2B, and S2C] and have correspondingly lower levels of surface TCRβ [Fig. 2A and 2C]. The extent of the stage-specific T cell development defects in $Atm^{RX/RX}$ mice is similar to that of $Atm^{-/-}$ mice, suggesting that the residual ATM kinase activity in $Atm^{RX/RX}$ mice, if present, is not sufficient to support efficient TCRα rearrangement (10). The normal total thymocytes number coupled with the stage-specific developmental defects seen in $Atm^{RX/RX}$ mice is unique and suggests that there might be a TCR-independent component that underlies the reduced thymocyte number in $Atm^{-/-}$ mice, potentially rooted in early progenitor cells (10, 29). There are no measurable defects in the cellularity or the composition of B cells [Fig. 2D, 2E, and S2D] or the frequency of myeloid cells ($CD11b^{+}Gr1^{+}$) in either $Atm^{RX/RX}$ or $Atm^{-/-}$ mice [Fig. S2E and S2F]. Mechanistically, $Atm^{RX/RX}$ lymphocytes accumulate abnormally high levels of hybrid joints (HJ) at TCRβ locus in T cells [Fig. 2F] and Igκ in B cells [Fig. 2G, S2G] like documented in $Atm^{-/-}$ mice (12).

IgH Immunoglobulin class switch recombination is compromised in $Atm^{RX/RX}$ B cells.

Purified $Atm^{RX/RX}$ as well as $Atm^{-/-}$ Psplenic B cells underwent IgG1 switching in the presence of anti-CD40 and IL-4 at ~50% reduced frequency as the wild-type control [Fig. 3A and 3B]. CTV is a cell surface dye, which can mark cell division by reduced surface levels. Analyses of IgG1 switching levels by CTV in $Atm^{RX/RX}$ and $Atm^{-/-}$ PB lymphocytes confirmed that reduced CSR cannot be explained by proliferation defects [Fig. 3C and 3D]. Using a telomere specific FISH probe that enhances the sensitivity to detect IgH locus breaks at the telomeric end of Chr12 (22), we found that the genomic instability of activating $Atm^{RX/RX}$ B cells is significantly lower than that of $Atm^{-/-}$ PB cells [Fig. 3E]. Telomeric FISH can identify two types of DNA breaks – chromosome breaks involving both sister chromatids and chromatid breaks involving one of the two sister chromatids [Fig. 3F]. While chromatid breaks occur during or after DNA replication, chromosome breaks might occur in G1 cells (22). Since CSR is initiated in the G1 phase of the cell cycle, CSR associated IgH breaks make up the majority of chromosome breaks in activating $Atm^{-/-}$ B cells (22). Most instabilities in $Atm^{RX/RX}$ B cells were chromosome breaks [Fig. 3G]. Proportional reduction of both chromosome and chromatid breaks in the metaphases from $Atm^{RX/RX}$ B cells together with the severe CSR defects suggests that the residual ATM kinase activity in $Atm^{RX/RX}$ cells might activate a cell cycle checkpoint to prevent the damaged cells from entering metaphase without restoring CSR.

CSR junction analyses reveal increased translocations and enrichment for microhomology from both *Atm*$^{RX/RX}$ and *Atm*$^{-/-}$ B cells.

To determine how ATM-RX protein affects the repair phase of CSR, we analyzed thousands of CSR and internal deletion junctions from activated *Atm*$^{RX/RX}$, *Atm*$^{+/+}$, and *Atm*$^{-/-}$ Pcontrol B cells using the high-throughput genome-wide translocation sequencing (HTGTS) technology developed by the laboratory of Dr. Frederick Alt (54, 57, 62, 63). Specifically, we placed the linear amplification primer near the 5' Sμ region (bait breaks) and isolated Sμ-Sμ junctions corresponding to internal deletion, as well as Sμ-Sγ1 and Sμ-Sε junctions corresponding to IgG1 and IgE CSR, respectively [Fig. 4A]. The translocation partners of the initial Sμ breaks are referred to as the preys, as they were called in the original HTGTS publications (52, 54). In addition to the location of the preys, HTGTS identified the orientation of junctions (Watson or Crick strands) based on the orientation of the junctional sequences. We defined the prey orientation as plus if it aligned from centromere to telomere starting from the junction site (as blue arrowheads in Fig. 4A) and as minus if it aligned from telomere to centromere starting from the junction site (as red arrowheads in Fig. 4A). Since the IgH locus resides at the minus strand of murine chromosome 12, the productive Sμ (telomeric) to Sγ1 or Sε (centromeric) joints are minus. The plus orientation joints can be generated by true inversion or could be inter-sister or inter-homology translocation between the Sμ breaks from one chromosome to the Sγ1 breaks on another chromosome 12 (sister or homology). This is due to the limitation that the digital genome is haploid while the physical genome is diploid. We are not able to distinguish the two homologous chromosomes in this pure background strain. As previously described for *Atm*$^{-/-}$ Pcells (19), the IgH junctions recovered from *Atm*$^{RX/RX}$ PB cells show an increased proportion of plus orientated joins, suggesting increased inter-chromosomal translocations (Fig. 4B). This trend of increased IgH+ oriented junctions holds for each switch region (Sμ, Sγ1, and Sε) analyzed as well (Fig. S3A). In *Atm*$^{+/+}$ B cells, about 30% of the IgH preys (both orientations) reside in each of the three switch regions analyzed Sμ, Sγ1, and Sε [Fig. 4C]. Loss of ATM and the R3057X mutation preferentially reduced Sμ-Sε junctions, while correspondingly increased Sμ-Sμ internal deletions [Fig. 4C]. Similar trends were also noted in other cNHEJ-deficient B cells (19, 54, 57, 64). In adult B cells, the majority of the IgE switching is achieved through sequential switching to Sγ1 first, then to Sε (65). This need for two end-ligation events might explain the hypersensitivity of IgE switching to DNA repair defects. Finally, CSR junctions recovered from ATM-deficient cells have increased the usage of microhomology at the junctions. Junctions recovered from *Atm*$^{-/-}$ and *Atm*$^{RX/RX}$ PB cells show similar skews toward short MHs in IgH together or in each switch region [Fig. 4D, S3B and S3C]. The number of Sμ-Sε junctions was too low for microhomology analyses. Together, the increased translocation (+ oriented junction), preferential loss of Sμ-Sε junctions, and the increased MH usage in the HTGTS analyses of *Atm*$^{RX/RX}$ PB cells indicate that the R3057X mutation impairs the DNA repair function of ATM during CSR, similar to the loss of ATM.

Spontaneous lymphomas in *Atm*$^{RX/RX}$ mice were significantly delayed compared to Atm$^{-/-}$ *mice*

Atm$^{-/-}$ mice routinely succumb to thymic lymphomas by 4 months of age (10). Despite similar T cell development and CSR defects, *Atm*$^{RX/RX}$ mice developed thymic lymphomas

nearly 140 days later than $Atm^{-/-}$ mice ($t_{1/2}$=115 days for $Atm^{-/-}$ vs. $t_{1/2}$= 255 days for $Atm^{RX/RX}$, p<0.002, Mantel-Cox test) [Fig. 5A]. Since $Atm^{+/+}$ mice in the pure 129sv background rarely develop spontaneous tumors by 365 days of age (1 year) (66, 67), these findings suggest that ATM-RX protein has a reduced tumor suppression function but some residual activity of ATM-RX can effectively delay lymphomagenesis. All $Atm^{RX/RX}$ mice analyzed succumbed to thymic lymphomas formed by immature (surface TCRβ low) T cells [Fig. 5B], like previously characterized $Atm^{-/-}$ mice (10, 29). Together with the lack of major genomic instability in the metaphases from activated $Atm^{RX/RX}$ B cells, these results suggest that the residual ATM-RX protein might have checkpoint functions that delay lymphomas and prevent cells with broken chromosomes from entering mitosis.

The residual ATM-R3057X protein maintain some radiation-induced checkpoint functions

To understand whether $Atm^{RX/RX}$ cells have residual ATM kinase activity, we measured irradiation (IR)-induced phosphorylation of ATM substrates in $Atm^{RX/RX}$ B cells together with $Atm^{-/-}$ and $Atm^{+/+}$ controls. IR induced phosphorylation of Kap1, a relatively specific substrate of ATM (68), is much reduced in $Atm^{RX/RX}$ cells, comparable to $Atm^{-/-}$ control [Fig. 6A-6D]. The residual radiation-induced Kap1 phosphorylation in $Atm^{RX/RX}$ and $Atm^{-/-}$ cells can be completely eliminated by DNA-PKcs inhibitor (NU7441, 15μM) [Fig. 6C, S4A, and S4C]. ATM inhibitor (KU55933 15 μM) also significantly reduced the residual KAP1 phosphorylation in $Atm^{RX/RX}$ [Fig. 6C and S4A]. But since KU55933 (15 μM) also consistently reduced Kap1 phosphorylation in $Atm^{-/-}$ cells [Fig. 6C, S4A, and S4C], we propose that this might be due to cross inhibition of DNA-PKcs (IC50 2.5 μM in the cell-free assay). Long exposure of the Western blot saturates the signal and made it less obvious [Fig. S4C]. The residual phosphorylation of two other ATM substrates – Chk2 and H2AX are also comparable between $Atm^{RX/RX}$ and $Atm^{-/-}$ cells [Fig. 6A, 6B, 6C, and S4A-C]. We reason that Western blotting might not be sensitive enough to measure residual ATM kinase activity. To directly measure DNA damage-induced G2/M checkpoint activation, we treated $Atm^{RX/RX}$ primary B cells with the radiation mimetic agent NCS (100 ng/mL) for 1 hour and performed BrdU labeling to identify G2/M cells (BrdU- 4N cells), and stained for Histone H3 Ser10 phosphorylation ($pH3^+$), a mitotic marker [Fig. 6E]. The frequency of G2/M cells and the percentage of mitotic $pH3^+$ positive cells among the G2/M cell population are comparable in untreated $Atm^{RX/RX}$, $Atm^{-/-}$, and $Atm^{+/+}$ cells [Fig. 6E and 6F]. As expected, based on literature, loss of ATM severely compromised the radiation-induced G2/M checkpoint [Fig. 6F and 6G]. $Atm^{RX/RX}$ cells show significantly more robust G2 arrest than $Atm^{-/-}$ cells [Fig. 6F and 6G], suggesting residual checkpoint activities, which might contribute to the delayed lymphomas and lack of measurable instability in metaphase preps. Next, we measured ROS induced activation of ATM by treating cells with tert-Butyl hydroperoxide (TBH), a relatively stable ROS inducer. We observed no ATM-dependent residual phosphorylation of Kap1, Chk2, or H2AX in $Atm^{RX/RX}$ cells, consistent with the lack of ROS induced activation of purified human ATM-R3047X protein (31) [Fig. 6H]. Together, these results suggest that the residual Atm-RX protein in the $Atm^{RX/RX}$ cells supports some DNA damage-induced G2/M checkpoints, but cannot be activated by ROS.

Discussion

Using knock-in mouse models, we found that a truncation mutation within the FATC domain (R3057X in mouse, corresponding to R3047X in human) destabilizes ATM protein, indicating a critical role of the FATC domain in ATM protein folding and stability. As such, $Atm^{RX/RX}$ mice display infertility, stage-specific T cell development defects, and CSR defects that are characteristic of ATM-null mice. However, in comparison to $Atm^{-/-}$ mice, $Atm^{RX/RX}$ mice have no growth retardation, nearly no thymus atrophy, substantially lower cytogenetic instability in metaphase, and much-delayed lymphomagenesis. These differences in phenotypes can be in part attributed to the residual DNA damage-induced checkpoint function of the ATM-RX protein. In this context, $Atm^{RX/RX}$ cells show no sign of ROS-induced activation of ATM, like previously described for A-T cells with compound ATM mutations including the R3047X (31, 69). Unfortunately, the severely reduced ATM-RX protein levels abrogate meiosis and lymphocyte development associated with DSB repairs, preventing us from analyzing the physiological role of ROS-dependent ATM activation. In this context, the patients carrying R3047X mutation also show 5–10 folds decrease of ATM protein levels, a mild form of A-T, primary immunodeficiency, and no lymphomas at the age of 20 (69). In the future, other separation of function mutations, if possible, would be needed to address the role of ROS induced ATM activation *in vivo*.

A-T is a heterogeneous disease. While all A-T patients develop different degrees of Ataxia, about 70% of A-T patients show immunodeficiency (3, 4), and 25% of patients develop lymphoid malignancies (28). The heterogeneity in A-T patients could be caused by the pleiotropic function of ATM kinase as a stress response kinase, and can also be influenced by the diverse genetic backgrounds and life experiences of individual patients. Inbred mouse models with knock-in mutations of ATM provide a valuable tool to address the heterogeneities associated with A-T. In the past three decades, 9 germline mouse models of A-T have been made, including 5 null alleles (5, 7, 8, 70, 71), 2 kinase-dead alleles (one knock-in (50) and one with BAC-transgene (72)), two auto-phosphorylation site alanine substitutions (both BAC transgenic) (73, 74), one in-frame deletion- deltaSRI (75), the R3047X described here, and the R3008H generated by us in another study(76). Among them, the auto-phosphorylation site mutation does not have any measurable impact on ATM kinase activity (73, 74). The phosphorylation site mutant mice are virtually identical to normal mice. The two mouse models expressing kinase-dead ATM result in embryonic lethality (50, 72), explaining why nearly all live-born A-T patients have truncating mutations with nearly no ATM protein expression. The deltaSRI, the R3047X, and R3008H all have substantially reduced kinase activities, manifested by infertility, and T cell development and CSR defects. Meanwhile, all three models have delayed lymphomagenesis, suggesting that the amount of ATM needed for its tumor suppressor function is much lower than that needed to support V(D)J or CSR recombination. Given the residual checkpoint function of ATM-R3057X detected here, the data suggests that ATM mediated phosphorylation of checkpoint targets, in particular G2/M targets CHK2 and CHK1, might be less vulnerable to ATM activity loss. It remains unclear whether this substrate selectively reflects a direct role of ATM on its substrates (*e.g.,* structure or activation difference) or reflects the signal amplification in the checkpoint pathway through

mediator kinases (*e.g.*, Chk1, Chk2, Wee1, etc.). Nevertheless, this finding highlights the important role of ATM-mediated checkpoint function in tumor suppression. In addition to lymphomagenesis, growth retardation and pan-lymphocytopenia can also be rescued with a minimal amount of ATM. This might be a feature to all hypomorphic ATM mutations, including but not limited to R3047X. Consistent with these observations, patients with residual ATM activity show mild phenotype, underlying the 70% immunodeficiency rate vs. 25% lymphoma rate in A-T patients. Systematic characterization of ATM missense mutations might be necessary to understand the full spectrum of A-T and how to prevent lethal lymphomas by restoring minimal ATM kinase activity that might not be visible by Western blotting, but detectable in cell cycle assays.

Finally, we note that ATM specific inhibitor KU55933 used at 15 μM has unexpected cross activity towards DNA-PKcs in murine cells. This effect is more obvious with low exposure, when the signals are not saturated. Lower dose of ATM kinase inhibitor, such as 7.5 μM should be considered for future experiments. We note the current experiments are conducted in murine B cells, whether similar dose also has off target effect in other cell types and in human cells remain elusive.

Supplementary Material

Refer to Web version on PubMed Central for supplementary material.

Acknowledgments

We thank all current and past members of the Zha lab for their helpful discussion. We thank Dr. Tanya Paull for discussing the R3047X allele and ATM biochemical analyses. The authors apologize to colleagues whose original work could not be cited due to space limitations and were covered by reviews instead.

Grant Support

This work was supported by the National Institutes of Health grants R01CA158073, R01CA215067, R01CA226852, and NIH P01CA174653 to S.Z. SZ is the recipient of the Leukemia Lymphoma Society Scholar Award. D.M. is a Leukemia Lymphoma Society Special Fellow. D.W and J.X were supported by NIH GM102362. This research was funded in part through the NIH/NCI Cancer Center Support Grant P30CA013696 to the Herbert Irving Comprehensive Cancer Center (HICCC) of Columbia University.

Reference

1. Shiloh Y. 2014. ATM: expanding roles as a chief guardian of genome stability. Exp Cell Res 329: 154–161. [PubMed: 25218947]
2. Lavin MF 2008. Ataxia-telangiectasia: from a rare disorder to a paradigm for cell signalling and cancer. Nat.Rev.Mol.Cell Biol 9: 759–769. [PubMed: 18813293]
3. Chopra C, Davies G, Taylor M, Anderson M, Bainbridge S, Tighe P, and McDermott EM 2014. Immune deficiency in Ataxia-Telangiectasia: a longitudinal study of 44 patients. Clinical and experimental immunology 176: 275–282. [PubMed: 24387201]
4. Nowak-Wegrzyn A, Crawford TO, Winkelstein JA, Carson KA, and Lederman HM 2004. Immunodeficiency and infections in ataxia-telangiectasia. J Pediatr 144: 505–511. [PubMed: 15069401]
5. Barlow C, Hirotsune S, Paylor R, Liyanage M, Eckhaus M, Collins F, Shiloh Y, Crawley JN, Ried T, Tagle D, and Wynshaw-Boris A. 1996. Atm-deficient mice: a paradigm of ataxia telangiectasia. Cell 86: 159–171. [PubMed: 8689683]

6. Elson A, Wang Y, Daugherty CJ, Morton CC, Zhou F, Campos-Torres J, and Leder P. 1996. Pleiotropic defects in ataxia-telangiectasia protein-deficient mice. Proc.Natl.Acad.Sci.U.S.A 93: 13084–13089. [PubMed: 8917548]
7. Xu Y, Ashley T, Brainerd EE, Bronson RT, Meyn MS, and Baltimore D. 1996. Targeted disruption of ATM leads to growth retardation, chromosomal fragmentation during meiosis, immune defects, and thymic lymphoma. Genes Dev. 10: 2411–2422. [PubMed: 8843194]
8. Borghesani PR, Alt FW, Bottaro A, Davidson L, Aksoy S, Rathbun GA, Roberts TM, Swat W, Segal RA, and Gu Y. 2000. Abnormal development of Purkinje cells and lymphocytes in Atm mutant mice. Proc.Natl.Acad.Sci.U.S.A 97: 3336–3341. [PubMed: 10716718]
9. Zha S, Sekiguchi J, Brush JW, Bassing CH, and Alt FW 2008. Complementary functions of ATM and H2AX in development and suppression of genomic instability. Proc.Natl.Acad.Sci.U.S.A 105: 9302–9306. [PubMed: 18599436]
10. Zha S, Bassing CH, Sanda T, Brush JW, Patel H, Goff PH, Murphy MM, Tepsuporn S, Gatti RA, Look AT, and Alt FW 2010. ATM-deficient thymic lymphoma is associated with aberrant tcrd rearrangement and gene amplification. Journal of Experimental Medicine 207: 1369–1380. [PubMed: 20566716]
11. Paull TT 2015. Mechanisms of ATM Activation. Annu Rev Biochem.
12. Bredemeyer AL, Sharma GG, Huang CY, Helmink BA, Walker LM, Khor KC, Nuskey B, Sullivan KE, Pandita TK, Bassing CH, and Sleckman BP 2006. ATM stabilizes DNA double-strand-break complexes during V(D)J recombination. Nature 442: 466–470. [PubMed: 16799570]
13. Zha S, Guo C, Boboila C, Oksenych V, Cheng HL, Zhang Y, Wesemann DR, Yuen G, Patel H, Goff PH, Dubois RL, and Alt FW 2011. ATM damage response and XLF repair factor are functionally redundant in joining DNA breaks. Nature 469: 250–254. [PubMed: 21160472]
14. Liu X, Jiang W, Dubois RL, Yamamoto K, Wolner Z, and Zha S. 2012. Overlapping functions between XLF repair protein and 53BP1 DNA damage response factor in end joining and lymphocyte development. Proc Natl Acad Sci U S A 109: 3903–3908. [PubMed: 22355127]
15. Li G, Alt FW, Cheng HL, Brush JW, Goff PH, Murphy MM, Franco S, Zhang Y, and Zha S. 2008. Lymphocyte-Specific Compensation for XLF/Cernunnos End-Joining Functions in V(D)J Recombination. Mol.Cell 31: 631–640. [PubMed: 18775323]
16. Oksenych V, Alt FW, Kumar V, Schwer B, Wesemann DR, Hansen E, Patel H, Su A, and Guo C. 2012. Functional redundancy between repair factor XLF and damage response mediator 53BP1 in V(D)J recombination and DNA repair. Proc Natl Acad Sci U S A 109: 2455–2460. [PubMed: 22308489]
17. Lumsden JM, McCarty T, Petiniot LK, Shen R, Barlow C, Wynn TA, Morse HC III, Gearhart PJ, Wynshaw-Boris A, Max EE, and Hodes RJ 2004. Immunoglobulin class switch recombination is impaired in Atm-deficient mice. J.Exp.Med 200: 1111–1121. [PubMed: 15504820]
18. Reina-San-Martin B, Chen HT, Nussenzweig A, and Nussenzweig MC 2004. ATM is required for efficient recombination between immunoglobulin switch regions. J.Exp.Med 200: 1103–1110. [PubMed: 15520243]
19. Panchakshari RA, Zhang X, Kumar V, Du Z, Wei PC, Kao J, Dong J, and Alt FW 2018. DNA double-strand break response factors influence end-joining features of IgH class switch and general translocation junctions. Proc Natl Acad Sci U S A 115: 762–767. [PubMed: 29311308]
20. Yu K, and Lieber MR 2019. Current insights into the mechanism of mammalian immunoglobulin class switch recombination. Crit Rev Biochem Mol Biol 54: 333–351. [PubMed: 31509023]
21. Pan-Hammarstrom Q, Lahdesmaki A, Zhao Y, Du L, Zhao Z, Wen S, Ruiz-Perez VL, Dunn-Walters DK, Goodship JA, and Hammarstrom L. 2006. Disparate roles of ATR and ATM in immunoglobulin class switch recombination and somatic hypermutation. J.Exp.Med 203: 99–110. [PubMed: 16390936]
22. Franco S, Gostissa M, Zha S, Lombard DB, Murphy MM, Zarrin AA, Yan C, Tepsuporn S, Morales JC, Adams MM, Lou Z, Bassing CH, Manis JP, Chen J, Carpenter PB, and Alt FW 2006. H2AX prevents DNA breaks from progressing to chromosome breaks and translocations. Mol.Cell 21: 201–214. [PubMed: 16427010]
23. Lange J, Pan J, Cole F, Thelen MP, Jasin M, and Keeney S. 2011. ATM controls meiotic double-strand-break formation. Nature 479: 237–240. [PubMed: 22002603]

24. Lange J, Yamada S, Tischfield SE, Pan J, Kim S, Zhu X, Socci ND, Jasin M, and Keeney S. 2016. The Landscape of Mouse Meiotic Double-Strand Break Formation, Processing, and Repair. Cell 167: 695–708 e616. [PubMed: 27745971]
25. Paiano J, Wu W, Yamada S, Sciascia N, Callen E, Paola Cotrim A, Deshpande RA, Maman Y, Day A, Paull TT, and Nussenzweig A. 2020. ATM and PRDM9 regulate SPO11-bound recombination intermediates during meiosis. Nat Commun 11: 857. [PubMed: 32051414]
26. Pacheco S, Marcet-Ortega M, Lange J, Jasin M, Keeney S, and Roig I. 2015. The ATM signaling cascade promotes recombination-dependent pachytene arrest in mouse spermatocytes. PLoS Genet 11: e1005017.
27. Kitagawa R, and Kastan MB 2005. The ATM-dependent DNA damage signaling pathway. Cold Spring Harb.Symp.Quant.Biol 70: 99–109. [PubMed: 16869743]
28. Morrell D, Cromartie E, and Swift M. 1986. Mortality and cancer incidence in 263 patients with ataxia-telangiectasia. J Natl Cancer Inst 77: 89–92. [PubMed: 3459930]
29. Jiang W, Lee BJ, Li C, Dubois RL, Gostissa M, Alt FW, and Zha S. 2015. Aberrant TCRdelta rearrangement underlies the T-cell lymphocytopenia and t(12;14) translocation associated with ATM deficiency. Blood 125: 2665–2668. [PubMed: 25721125]
30. Liyanage M, Weaver Z, Barlow C, Coleman A, Pankratz DG, Anderson S, Wynshaw-Boris A, and Ried T. 2000. Abnormal rearrangement within the alpha/delta T-cell receptor locus in lymphomas from Atm-deficient mice. Blood. 96: 1940–1946. [PubMed: 10961898]
31. Guo Z, Kozlov S, Lavin MF, Person MD, and Paull TT 2010. ATM activation by oxidative stress. Science 330: 517–521. [PubMed: 20966255]
32. Reichenbach J, Schubert R, Schwan C, Muller K, Bohles HJ, and Zielen S. 1999. Anti-oxidative capacity in patients with ataxia telangiectasia. Clin Exp Immunol 117: 535–539. [PubMed: 10469059]
33. Barlow C, Dennery PA, Shigenaga MK, Smith MA, Morrow JD, Roberts LJ, Wynshaw-Boris A, and Levine RL 1999. Loss of the ataxia-telangiectasia gene product causes oxidative damage in target organs. Proc.Natl.Acad.Sci.U.S.A 96: 9915–9919. [PubMed: 10449794]
34. Reichenbach J, Schubert R, Schindler D, Muller K, Bohles H, and Zielen S. 2002. Elevated oxidative stress in patients with ataxia telangiectasia. Antioxid Redox Signal 4: 465–469. [PubMed: 12215213]
35. Barzilai A, Rotman G, and Shiloh Y. 2002. ATM deficiency and oxidative stress: a new dimension of defective response to DNA damage. DNA Repair (Amst) 1: 3–25. [PubMed: 12509294]
36. McKinnon PJ 2017. Genome integrity and disease prevention in the nervous system. Genes Dev 31: 1180–1194. [PubMed: 28765160]
37. Lee JH, Mand MR, Kao CH, Zhou Y, Ryu SW, Richards AL, Coon JJ, and Paull TT 2018. ATM directs DNA damage responses and proteostasis via genetically separable pathways. Sci Signal 11.
38. Menolfi D, and Zha S. 2020. ATM, ATR and DNA-PKcs kinases-the lessons from the mouse models: inhibition not equal deletion. Cell Biosci 10: 8. [PubMed: 32015826]
39. Baretic D, and Williams RL 2014. PIKKs--the solenoid nest where partners and kinases meet. Curr Opin Struct Biol 29: 134–142. [PubMed: 25460276]
40. Yates LA, Williams RM, Hailemariam S, Ayala R, Burgers P, and Zhang X. 2020. Cryo-EM Structure of Nucleotide-Bound Tel1(ATM) Unravels the Molecular Basis of Inhibition and Structural Rationale for Disease-Associated Mutations. Structure 28: 96–104 e103. [PubMed: 31740029]
41. Wang X, Chu H, Lv M, Zhang Z, Qiu S, Liu H, Shen X, Wang W, and Cai G. 2016. Structure of the intact ATM/Tel1 kinase. Nat Commun 7: 11655. [PubMed: 27229179]
42. Wang X, Ran T, Zhang X, Xin J, Zhang Z, Wu T, Wang W, and Cai G. 2017. 3.9 A structure of the yeast Mec1-Ddc2 complex, a homolog of human ATR-ATRIP. Science 358: 1206–1209. [PubMed: 29191911]
43. Sun Y, Jiang X, Chen S, Fernandes N, and Price BD 2005. A role for the Tip60 histone acetyltransferase in the acetylation and activation of ATM. Proc Natl Acad Sci U S A 102: 13182–13187. [PubMed: 16141325]
44. Kozlov SV, Graham ME, Jakob B, Tobias F, Kijas AW, Tanuji M, Chen P, Robinson PJ, Taucher-Scholz G, Suzuki K, So S, Chen D, and Lavin MF 2011. Autophosphorylation and

ATM activation: additional sites add to the complexity. J Biol Chem 286: 9107–9119. [PubMed: 21149446]

45. Beamish HJ, Jessberger R, Riballo E, Priestley A, Blunt T, Kysela B, and Jeggo PA 2000. The C-terminal conserved domain of DNA-PKcs, missing in the SCID mouse, is required for kinase activity. Nucleic Acids Res. 28: 1506–1513. [PubMed: 10710416]
46. Yang H, Rudge DG, Koos JD, Vaidialingam B, Yang HJ, and Pavletich NP 2013. mTOR kinase structure, mechanism and regulation. Nature 497: 217–223. [PubMed: 23636326]
47. Zha S, Sekiguchi J, Brush JW, Bassing CH, and Alt FW 2008. Complementary functions of ATM and H2AX in development and suppression of genomic instability. Proc Natl Acad Sci U S A 105: 9302–9306. [PubMed: 18599436]
48. Liu X, Shao Z, Jiang W, Lee BJ, and Zha S. 2017. PAXX promotes KU accumulation at DNA breaks and is essential for end-joining in XLF-deficient mice. Nat Commun 8: 13816. [PubMed: 28051062]
49. Liu X, Wang XS, Lee BJ, Wu-Baer FK, Lin X, Shao Z, Estes VM, Gautier J, Baer R, and Zha S. 2019. CtIP is essential for early B cell proliferation and development in mice. J Exp Med 216: 1648–1663. [PubMed: 31097467]
50. Yamamoto K, Wang Y, Jiang W, Liu X, Dubois RL, Lin CS, Ludwig T, Bakkenist CJ, and Zha S. 2012. Kinase-dead ATM protein causes genomic instability and early embryonic lethality in mice. J Cell Biol 198: 305–313. [PubMed: 22869596]
51. Franco S, Gostissa M, Zha S, Lombard DB, Murphy MM, Zarrin AA, Yan C, Tepsuporn S, Morales JC, Adams MM, Lou Z, Bassing CH, Manis JP, Chen J, Carpenter PB, and Alt FW 2006. H2AX prevents DNA breaks from progressing to chromosome breaks and translocations. Mol Cell 21: 201–214. [PubMed: 16427010]
52. Hu J, Meyers RM, Dong J, Panchakshari RA, Alt FW, and Frock RL 2016. Detecting DNA double-stranded breaks in mammalian genomes by linear amplification-mediated high-throughput genome-wide translocation sequencing. Nat Protoc 11: 853–871. [PubMed: 27031497]
53. Crowe JL, Shao Z, Wang XS, Wei PC, Jiang W, Lee BJ, Estes VM, Alt FW, and Zha S. 2018. Kinase-dependent structural role of DNA-PKcs during immunoglobulin class switch recombination. Proc Natl Acad Sci U S A 115: 8615–8620. [PubMed: 30072430]
54. Dong J, Panchakshari RA, Zhang T, Zhang Y, Hu J, Volpi SA, Meyers RM, Ho YJ, Du Z, Robbiani DF, Meng F, Gostissa M, Nussenzweig MC, Manis JP, and Alt FW 2015. Orientation-specific joining of AID-initiated DNA breaks promotes antibody class switching. Nature 525: 134–139. [PubMed: 26308889]
55. Wang XS, Zhao J, Wu-Baer F, Shao Z, Lee BJ, Cupo OM, Rabadan R, Gautier J, Baer R, and Zha S. 2020. CtIP-mediated DNA resection is dispensable for IgH class switch recombination by alternative end-joining. Proc Natl Acad Sci U S A 117: 25700–25711. [PubMed: 32989150]
56. Faust GG, and Hall IM 2012. YAHA: fast and flexible long-read alignment with optimal breakpoint detection. Bioinformatics 28: 2417–2424. [PubMed: 22829624]
57. Crowe JL, Shao Z, Wang XS, Wei PC, Jiang W, Lee BJ, Estes VM, Alt FW, and Zha S. 2018. Kinase-dependent structural role of DNA-PKcs during immunoglobulin class switch recombination. Proc Natl Acad Sci U S A.
58. Crowe JL, Wang XS, Shao Z, Lee BJ, Estes VM, and Zha S. 2020. DNA-PKcs phosphorylation at the T2609 cluster alters the repair pathway choice during immunoglobulin class switch recombination. BioRxiv.
59. Andegeko Y, Moyal L, Mittelman L, Tsarfaty I, Shiloh Y, and Rotman G. 2001. Nuclear retention of ATM at sites of DNA double strand breaks. J Biol Chem 276: 38224–38230. [PubMed: 11454856]
60. Kurosaki T, Popp MW, and Maquat LE 2019. Quality and quantity control of gene expression by nonsense-mediated mRNA decay. Nat Rev Mol Cell Biol 20: 406–420. [PubMed: 30992545]
61. Xu Y. 1999. ATM in lymphoid development and tumorigenesis. Adv Immunol 72: 179–189. [PubMed: 10361575]
62. Hu J, Zhang Y, Zhao L, Frock RL, Du Z, Meyers RM, Meng FL, Schatz DG, and Alt FW 2015. Chromosomal Loop Domains Direct the Recombination of Antigen Receptor Genes. Cell 163: 947–959. [PubMed: 26593423]

63. Zhang Y, McCord RP, Ho YJ, Lajoie BR, Hildebrand DG, Simon AC, Becker MS, Alt FW, and Dekker J. 2012. Spatial organization of the mouse genome and its role in recurrent chromosomal translocations. Cell 148: 908–921. [PubMed: 22341456]
64. Wang XS, Lee BJ, and Zha S. 2020. The recent advances in non-homologous end-joining through the lens of lymphocyte development. DNA Repair (Amst) 94: 102874.
65. Tong P, and Wesemann DR 2015. Molecular Mechanisms of IgE Class Switch Recombination. Curr Top Microbiol Immunol 388: 21–37. [PubMed: 25553793]
66. Spring K, Cross S, Li C, Watters D, Ben-Senior L, Waring P, Ahangari F, Lu SL, Chen P, Misko I, Paterson C, Kay G, Smorodinsky NI, Shiloh Y, and Lavin MF 2001. Atm knock-in mice harboring an in-frame deletion corresponding to the human ATM 7636del9 common mutation exhibit a variant phenotype. Cancer Res 61: 4561–4568. [PubMed: 11389091]
67. Armata HL, Shroff P, Garlick DE, Penta K, Tapper AR, and Sluss HK 2011. Loss of p53 Ser18 and Atm results in embryonic lethality without cooperation in tumorigenesis. PLoS One 6: e24813.
68. Ziv Y, Bielopolski D, Galanty Y, Lukas C, Taya Y, Schultz DC, Lukas J, Bekker-Jensen S, Bartek J, and Shiloh Y. 2006. Chromatin relaxation in response to DNA double-strand breaks is modulated by a novel ATM- and KAP-1 dependent pathway. Nat Cell Biol 8: 870–876. [PubMed: 16862143]
69. Gilad S, Chessa L, Khosravi R, Russell P, Galanty Y, Piane M, Gatti RA, Jorgensen TJ, Shiloh Y, and Bar-Shira A. 1998. Genotype-phenotype relationships in ataxia-telangiectasia and variants. Am J Hum Genet 62: 551–561. [PubMed: 9497252]
70. Westphal CH, Rowan S, Schmaltz C, Elson A, Fisher DE, and Leder P. 1997. atm and p53 cooperate in apoptosis and suppression of tumorigenesis, but not in resistance to acute radiation toxicity. Nat.Genet 16: 397–401. [PubMed: 9241281]
71. Herzog KH, Chong MJ, Kapsetaki M, Morgan JI, and McKinnon PJ 1998. Requirement for Atm in ionizing radiation-induced cell death in the developing central nervous system. Science 280: 1089–1091. [PubMed: 9582124]
72. Daniel JA, Pellegrini M, Lee BS, Guo Z, Filsuf D, Belkina NV, You Z, Paull TT, Sleckman BP, Feigenbaum L, and Nussenzweig A. 2012. Loss of ATM kinase activity leads to embryonic lethality in mice. J Cell Biol 198: 295–304. [PubMed: 22869595]
73. Daniel JA, Pellegrini M, Lee JH, Paull TT, Feigenbaum L, and Nussenzweig A. 2008. Multiple autophosphorylation sites are dispensable for murine ATM activation in vivo. J.Cell Biol 183: 777–783. [PubMed: 19047460]
74. Pellegrini M, Celeste A, Difilippantonio S, Guo R, Wang W, Feigenbaum L, and Nussenzweig A. 2006. Autophosphorylation at serine 1987 is dispensable for murine Atm activation in vivo. Nature.
75. Peng Y, Woods RG, Beamish H, Ye R, Lees-Miller SP, Lavin MF, and Bedford JS 2005. Deficiency in the catalytic subunit of DNA-dependent protein kinase causes down-regulation of ATM. Cancer Res 65: 1670–1677. [PubMed: 15753361]
76. Milanovic M, Houghton LM, Menolfi D, Lee JH, Yamamoto K, Li Y, Lee BJ, Xu J, Estes VM, Wang D, McKinnon PJ, Paull TT, and Zha S. 2020. The cancer-associated ATM R3008H mutation reveals the link between ATM activation and its exchange. Cancer Res. Online ahead of print.

Key points:

- The FATC domain is critical for ATM protein stability *in vivo*.
- R3047X mutation in ATM FATC domain blocks lymphocyte development.
- ATM-R3047X has compromised tumor suppression functions.

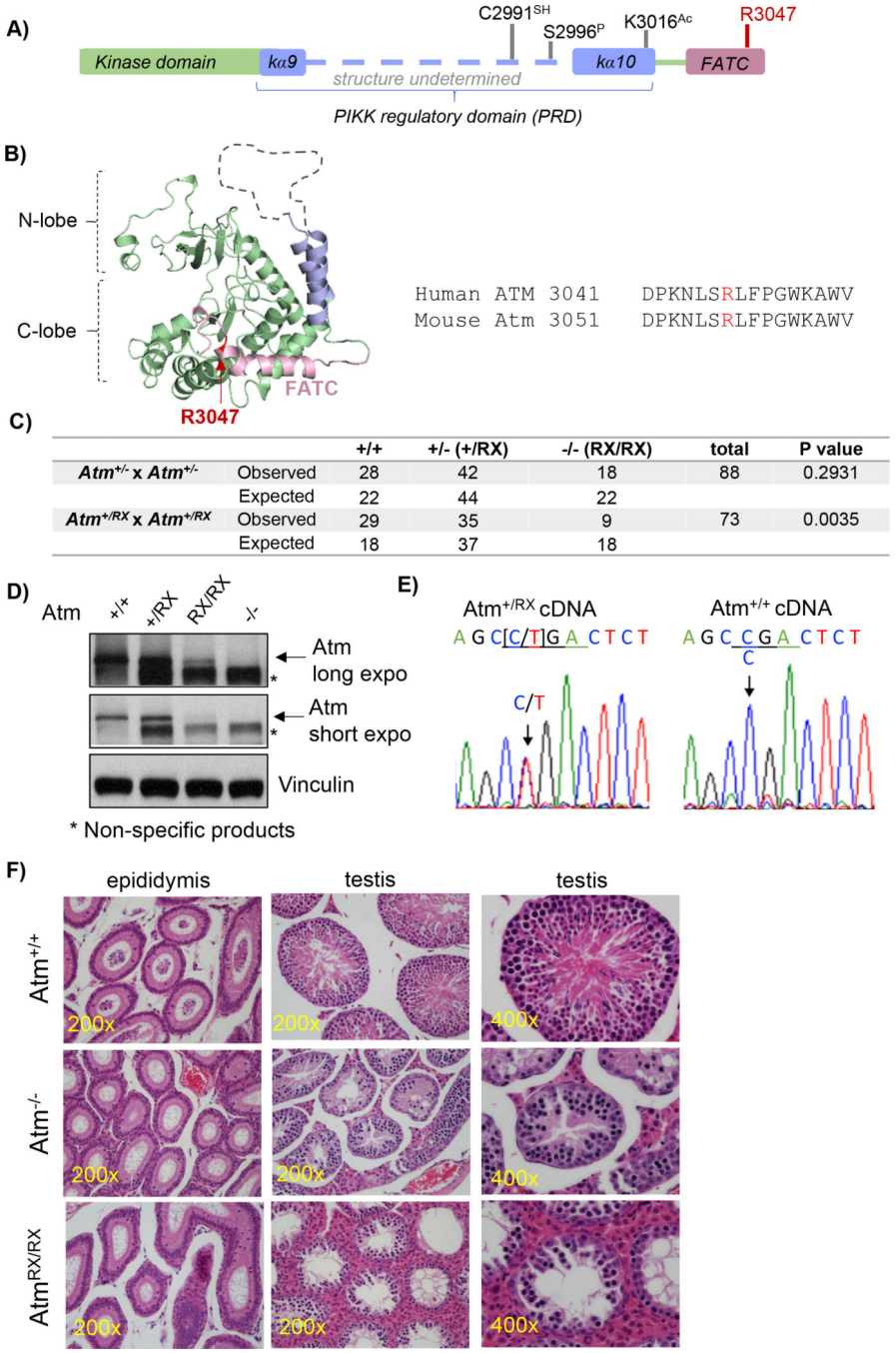

		+/+	+/- (+/RX)	-/- (RX/RX)	total	P value
***Atm*$^{+/-}$ x *Atm*$^{+/-}$**	Observed	28	42	18	88	0.2931
	Expected	22	44	22		
***Atm*$^{+/RX}$ x *Atm*$^{+/RX}$**	Observed	29	35	9	73	0.0035
	Expected	18	37	18		

Fig 1. Generation and characterization of ATM R3047X mouse model

A) Schematic representation of human ATM kinase and its C-terminal portion showing the kinase domain, protein regulatory domain (PRD) with Kα9 and Kα10 helices, and the FATC domain with the approximate position of the residue R3047. **B)** The in-silico structure model of ATM kinase domain derived from mTOR kinase. The color code is corresponding to Fig.1A. Kinase domain, pastel green; kα9 and kα10 helices, pastel violet; PRD, grey broken line; FATC domain, pastel pink. The targeted residue R3047 is in red. On the right is the alignment of the mouse and human sequences surrounding the R3047 residue. **C)** Expected

and observed genotypes from an intercross between $Atm^{+/-}$ (top two rows) or $Atm^{+/RX}$ mice. The p-value was calculated using the χ^2 test. **D)** Western blot analysis of Atm-RX protein expression in littermate matched v-abl kinase transformed B cells. **E)** The Atm^{RX} transcript levels are comparable to $Atm^{+/+}$. The expression of the mutated R3057X allele was confirmed by the sequencing of reverse-transcribed cDNA extracted from $Atm^{+/Rx}$ cells. **F)** Representative histological sections of H&E staining of epididymis and testis of $Atm^{+/+}$, $Atm^{-/-}$, and $Atm^{RX/RX}$ mice.

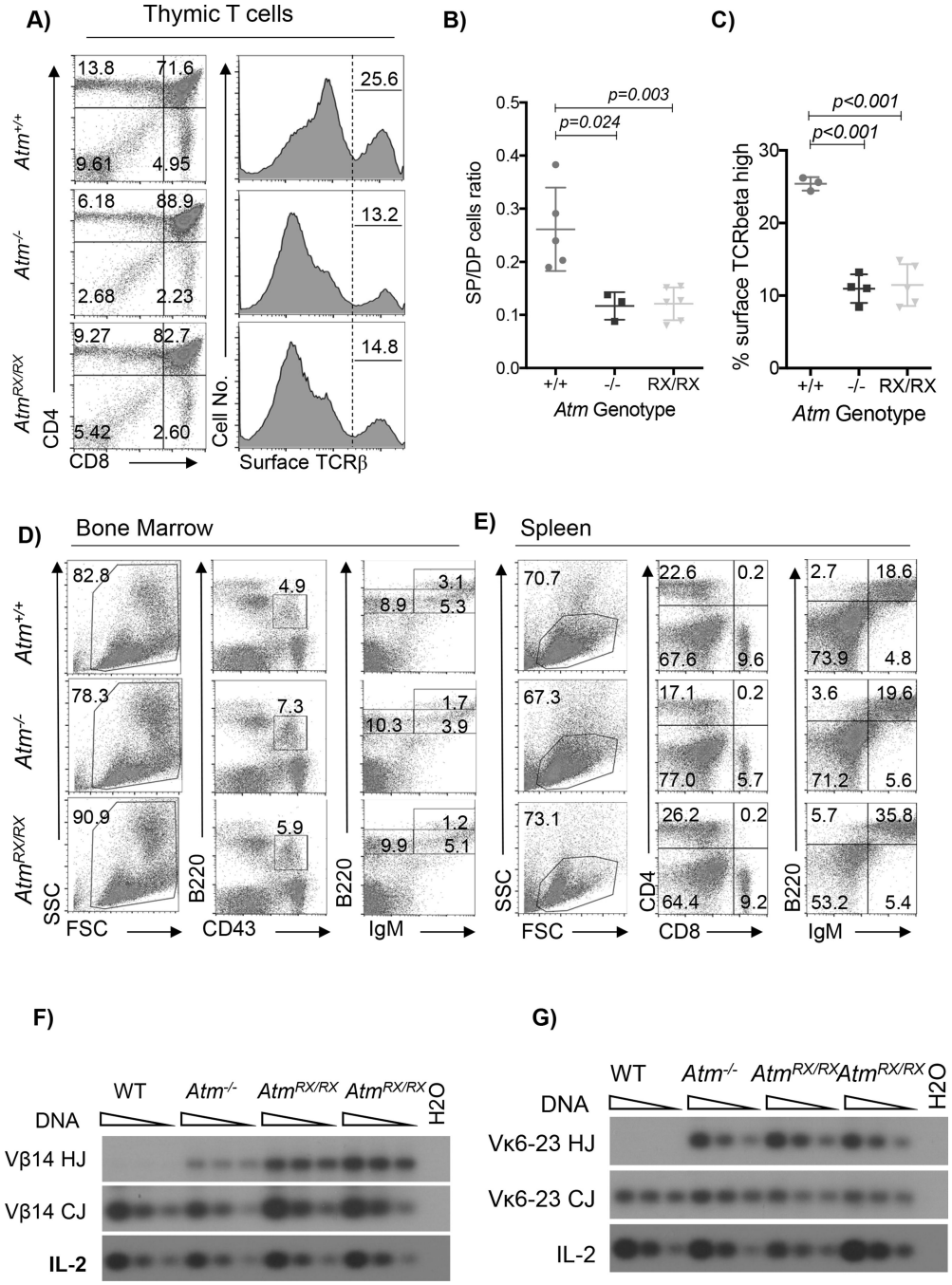

Fig 2. Immature T cell development is impaired in *Atm*$^{RX/RX}$ mice

A) Representative flow cytometry analyses of thymocytes from *Atm*$^{+/+}$, *Atm* $^{-/-}$, and *Atm*$^{RX/RX}$ mice. The percentage of cells in each quadrant is marked on the plots. The dotted line shows the percentage of high surface TCRβ. **B)** Ratios of the total single-positive cells (CD8+CD4− or CD8-CD4+) to double-positive (CD8+CD4+) T cells for *Atm*$^{+/+}$ (n=5) *Atm*$^{-/-}$ (n=3), and *Atm*$^{RX/RX}$ (n=6) mice. On the graphs, horizontal lines represent mean ± standard deviation. P-values were calculated using unpaired two-tailed Student's t-test. **C)** Percentages of cell populations expressing high-level surface TCRβ in 6–8 week

old *Atm*$^{+/+}$, *Atm*$^{-/-}$, and *Atm*$^{RX/RX}$ mice (n>=3 for each genotype). Horizontal lines on the plots represent mean ± standard deviation. P-values were calculated using unpaired two-tailed Student's t-test. **D)** Representative flow cytometry analyses of B cells in bone marrow from *Atm*$^{+/+}$, *Atm*$^{-/-}$ and *Atm*$^{RX/RX}$ mice. The percentage of cells in each quadrant is marked on the plots. **E)** Representative flow cytometry analyses of T cell (middle) and B cell (right) markers in spleen from *Atm*$^{+/+}$, *Atm*$^{-/-}$, and *Atm*$^{RX/RX}$ mice. The percentage of cells in each quadrant is marked on the plots. **F)** Southern Blot analyses of coding joints (CJ) and hybrid joints (HJ) involving Vβ14 at the TCRβ locus. IL-2 locus was used as the loading control. The DNA was harvest from thymocytes of two independent *Atm*$^{RX/RX}$ mice and control *Atm*$^{+/+}$ and *Atm*$^{-/-}$ mice. The dilution factor is 4. **G)** Southern Blot analyses of coding joints (CJ) and hybrid joints (HJ) involving Vκ6–23 at the Igκ locus. IL-2 locus was used as the loading control. The DNA was harvest from the spleen of two independent *Atm*$^{RX/RX}$ mice and control *Atm*$^{+/+}$ and *Atm*$^{-/-}$ mice. The diagram of the Vκ6–23 locus arrangement is in Supplementary Figure 2G.

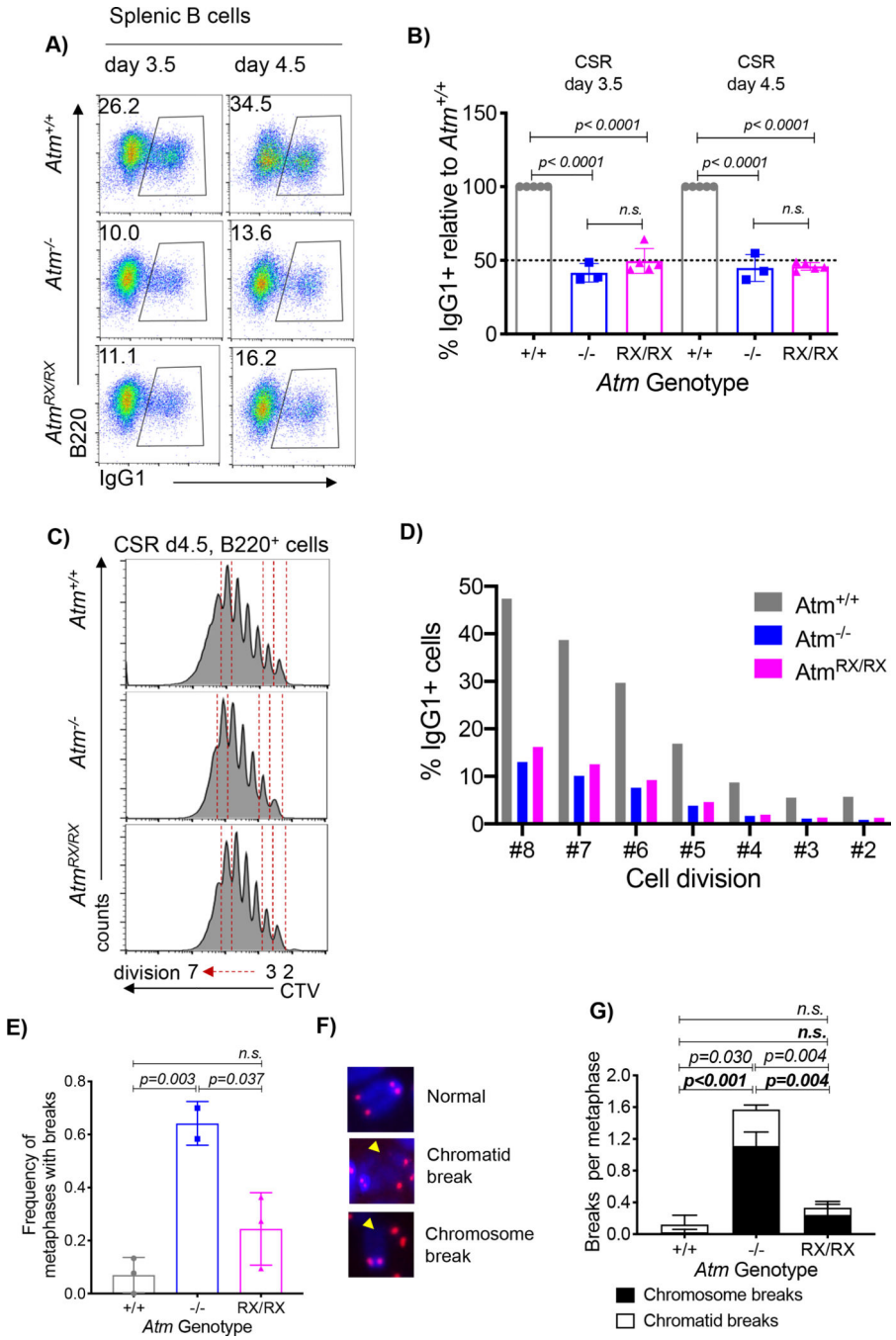

Fig 3. *Atm*$^{RX/RX}$ mice have defects in B cell CSR comparable to *Atm*$^{-/-}$ mice

A) Representative flow cytometry plots for surface IgG1+ frequency in activated B cells. **B)** The percentage of IgG1+ B cells (relative to WT cells in each experiment; WT set as 100%) in *Atm*$^{+/+}$ (n=5), *Atm*$^{-/-}$ (n=3), and *Atm*$^{RX/RX}$ (n=5) B cells. Bar graphs represent the mean ± standard deviation. P-values were calculated using unpaired two-tailed Student's t-test. Dotted line indicates 50% of IgG1 switching detected in WT cells. **C)** Proliferation of activated *Atm*$^{+/+}$, *Atm*$^{-/-}$, and *Atm*$^{RX/RX}$ B cells stained with CTV. Representative flow cytometry histograms with annotated cell divisions for each indicated genotype are shown.

Dotted lines indicate divisions 2, 3, and 7 as an illustration for cell population gating. **D)** CTV proliferation analysis of IgG1+ B cells from $Atm^{+/+}$, $Atm^{-/-}$, and $Atm^{RX/RX}$ mice subdivided by cell division. The bar graphs represent the percentage of IgG1+ B cells with indicated cell division. Bar graphs show one representative experiment. **E)** Frequency of metaphases with cytogenetic abnormalities in splenic B cells of the indicated genotypes. Bar graphs represent mean ± standard deviation (n>= 2). P-values were calculated using unpaired two-tailed Student's *t*-test. **F)** Illustrations of the two types of cytogenetic abnormalities scored. **G)** Frequency of chromatid and chromosome breaks per metaphase in $Atm^{+/+}$, $Atm^{-/-}$, or $Atm^{RX/RX}$ B cells at day 4.5 of the CSR assay. Bar graphs represent mean ± standard deviation (n>= 2). P-values were calculated using unpaired two-tailed Student's *t*-test. P-values in bold refer to statistics for chromosome breaks.

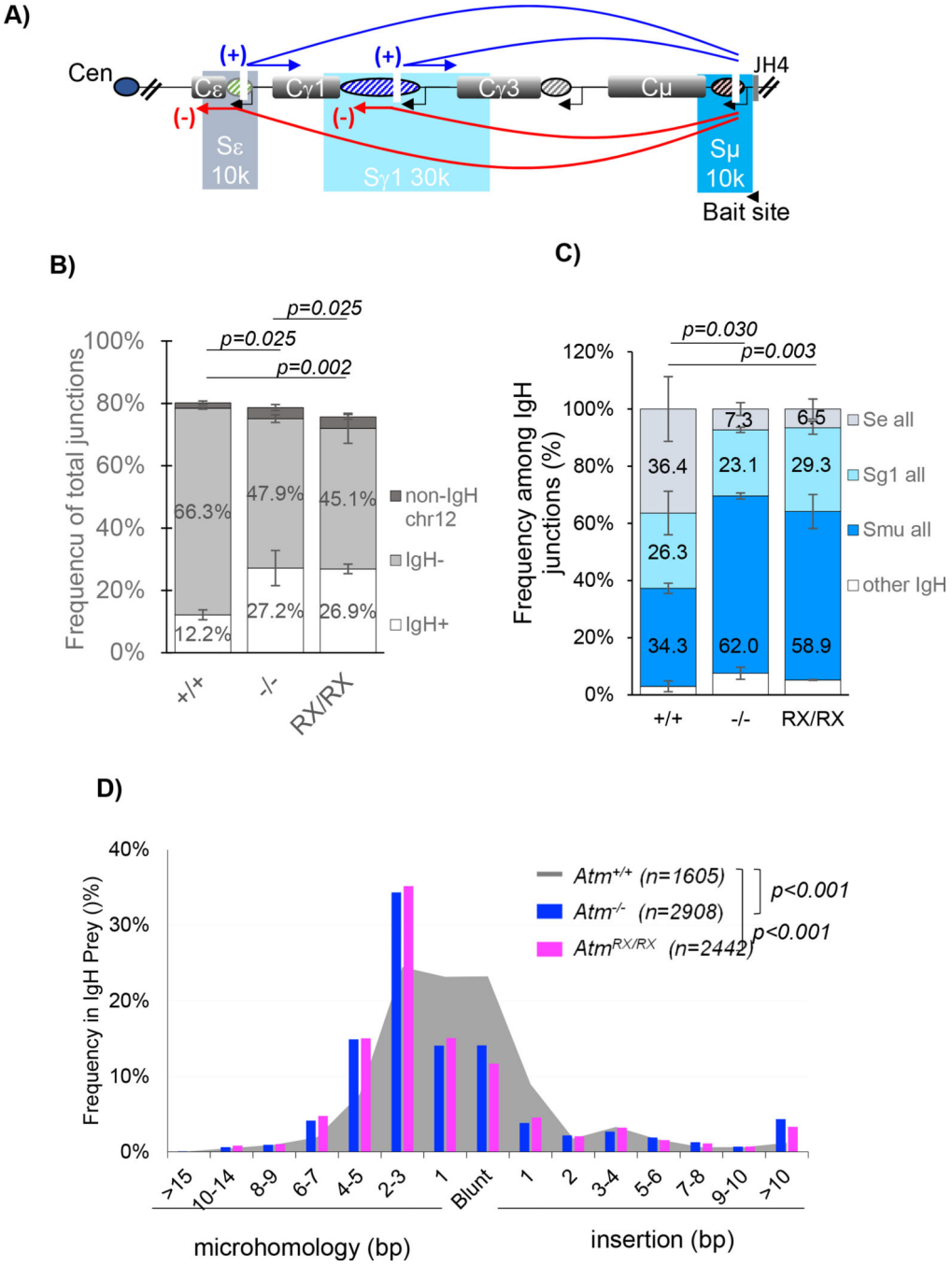

Fig 4. HTGTS analysis of stimulated *Atm*$^{RX/RX}$ B lymphocytes

A) Diagram of representative preys identified in HTGTS using a common bait at the 5'Sμ region. The centromere (Cen) and JH4 exon (closer to telomere) are marked. The red arrows indicate the possible configuration of (–) strand/deletional prey sites and blue arrows indicate the possible configuration of (+) strand/inversional prey sites. The approximate sizes of switch regions are marked in blue for the Sμ, in cyan for Sγ1, and in grey for Sε switch region. **B)** Staggered bars represent frequencies of HTGTS identified prey-break sites including IgH (+) in white, IgH (–) in light gray, and non-IgH but still within chromosome

12 in dark gray. Data represent the mean ± standard deviation of two independently derived libraries from *Atm*$^{+/+}$, *Atm*$^{-/-}$, or *Atm*$^{RX/RX}$ B cells at day 4 of the CSR assay. P-values were calculated using unpaired two-tailed Student's t-test and refer to statistics for IgH (–) prey-break sites. **C)** The relative frequency of prey break sites in Sμ, Sγ1, Sε and other IgH regions among all IgH prey sites. Data represent the mean ± standard deviation of two independently derived libraries. P-values were calculated using unpaired two-tailed Student's t-test and refer to statistics for prey break sites in the Sμ switch region. **D)** The distribution of IgH junctions by microhomology (MH) or insertion (INS). The graph represents the pooled IgH junctions from two libraries from two independent mice of each genotype. P-values were calculated using the Kolmogorov–Smirnov test.

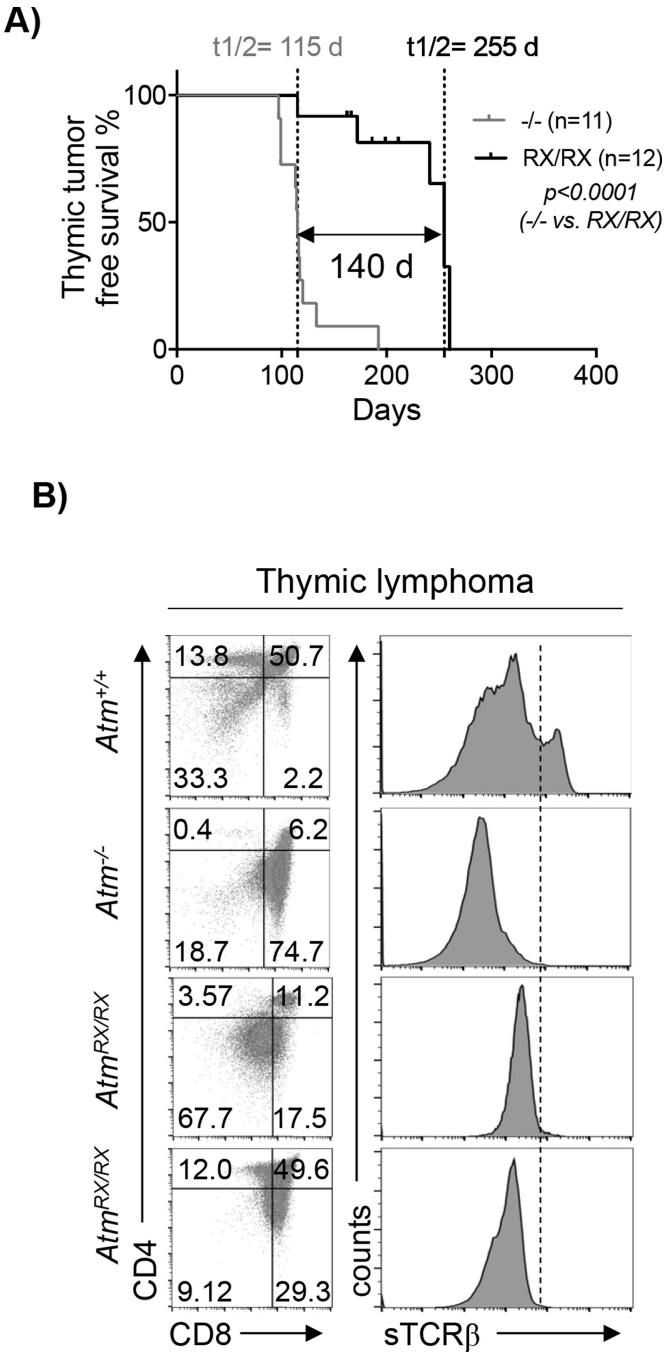

Fig 5. *Atm*$^{RX/RX}$ mice develop thymic lymphoma later than *Atm*$^{-/-}$ mice

A) Kaplan-Meier survival curve of *Atm*$^{-/-}$ and *Atm*$^{RX/RX}$ mice. The $t_{1/2}$ for total tumor-free survival is 115 days for *Atm*$^{-/-}$ and 255 days *Atm*$^{RX/RX}$ mice. The $\Delta t_{1/2}$ =140 days between *Atm*$^{-/-}$ and *Atm*$^{RX/RX}$ cohorts. Mantel-Cox/log-rank test was used for statistical analysis. **E)** Representative FACS analysis of immature thymic lymphomas from *Atm*$^{-/-}$ and *Atm*$^{RX/RX}$ mice.

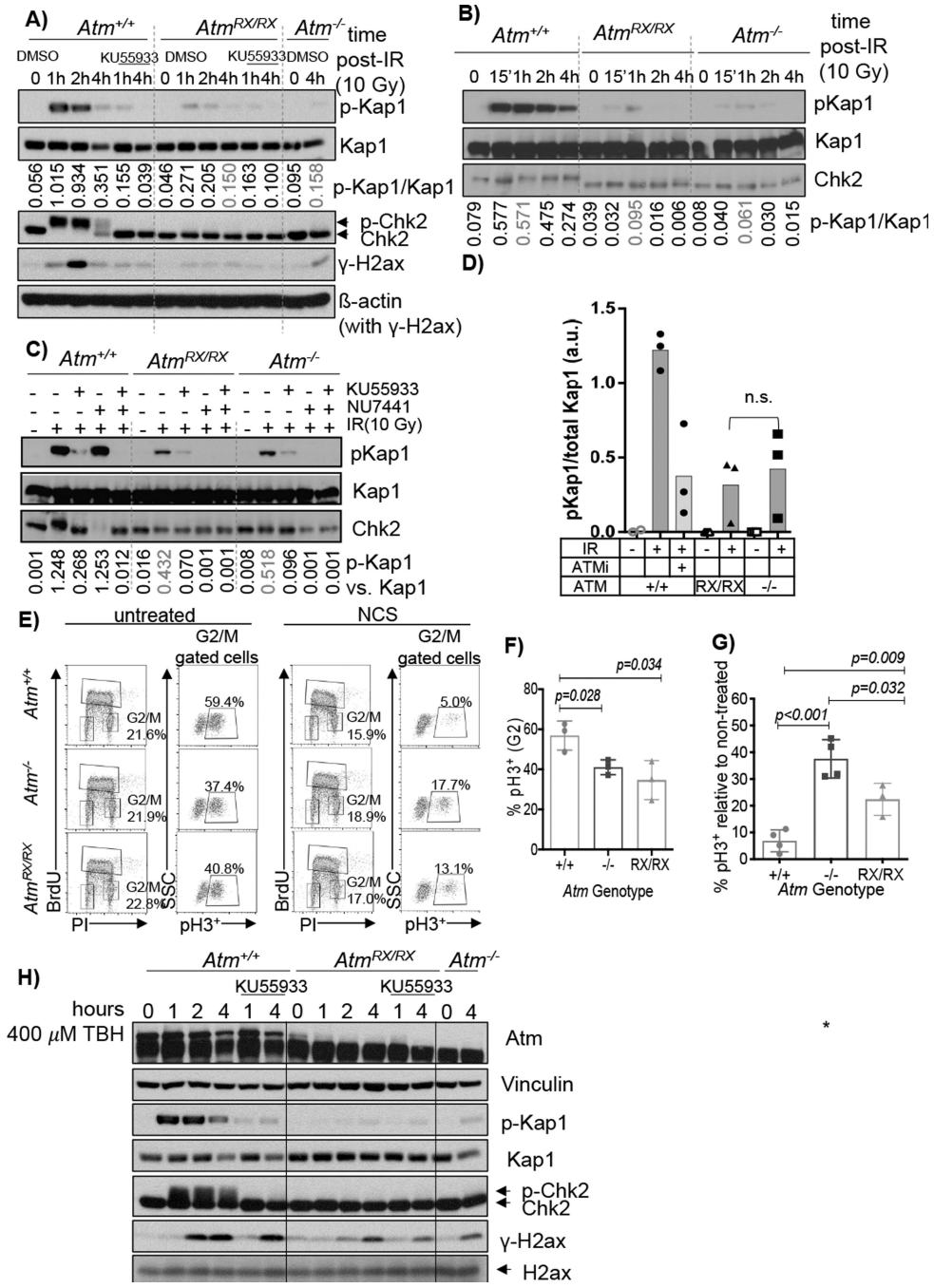

Fig 6. Residual ATM-RX protein retains checkpoint functions

A) Immunoblot analysis of $Atm^{+/+}$, $Atm^{RX/RX}$, and $Atm^{-/-}$ v-abl kinase transformed B cells 1, 2, and 4 hours after 10 Gy irradiation. ATM inhibitor Ku55933 (15μM) was added 1-hour before irradiation. **B)** Immunoblot analysis of $Atm^{+/+}$, $Atm^{RX/RX}$, and $Atm^{-/-}$ primary splenic B cells at 15 minutes and 1, 2, and 4 hours after 10 Gy irradiation. **C)** Immunoblot analysis of $Atm^{+/+}$, $Atm^{RX/RX}$, and $Atm^{-/-}$ primary splenic B cells at 2-hours after 10 Gy irradiation. ATM inhibitor Ku55933, DNA-PKcs inhibitor NU7441 (15μM) were added 1-hour before IR. A), B) and C) IR-induced phosphorylation assays were done twice in

primary B cells and three times in v-abl kinase transformed B cells. Immunoblots from one of the two experiments are shown. **D)** Quantification of the relative intensity of pKap1/total Kap1 in v-abl kinase transformed B cells. The data summarized the results from Figure 6C, S4A, and S4C. **E)** Representative flow cytometry analyses of the general cell cycle and the frequency of $pH3^+$ cells with or without pulse damage by NCS (100 ng/mL for 1-hour). **F)** The frequency of $pH3^+$ cells from all G2/M (4N) cells in activated B cells (n>=3 for each genotype). The bar graphs show mean ± standard deviation. P-values were calculated using the unpaired two-tailed Student's t-test. **G)** Bar graphs represent the percentages of $pH3^+$ NCS treated cells relative to non-treated cells. The bar graphs show mean ± standard deviation. P-values were calculated using the unpaired two-tailed Student's t-test (n>=3). **H)** Western blot analysis of v-abl kinase transformed B cells treated with the ROS-inducing agent TBH (400μM). Cells were collected at the indicated times after TBH treatment. ATM inhibitor Ku55933 (final concentration of 15μM) was added 1-hour before TBH addition.